Journal of Solid State Chemistry 317 (2023) 123667

Contents lists available at ScienceDirect

Journal of Solid State Chemistry

journal homepage: www.elsevier.com/locate/jssc

Structure and magnetism across the $Sr_{2-x}Ba_xNiOsO_6$ phase diagram: Understanding magnetic superexchange between first and third row transition metal ions

Phuong M. Tran [a], John S.O. Evans [b], Patrick M. Woodward [a,*]

[a] Department of Chemistry and Biochemistry, The Ohio State University, 100 W. 18th Avenue, Columbus, OH, 43210, United States
[b] Department of Chemistry, University Science Site, Durham University, South Road, Durham, DH1 3LE, United Kingdom

ARTICLE INFO

Keywords:
Double perovskite
5d Transition metal oxide
Ferrimagnetism
Spin glass
Superexchange

ABSTRACT

The crystal chemistry and magnetism of compositions in the $Sr_{2-x}Ba_xNiOsO_6$ phase diagram have been investigated to better understand the superexchange interactions between 3d and 5d transition metal ions. Compositions with $x < 1.35$ crystallize with the double perovskite structure, while those with $x > 1.83$ crystallize in a trigonal structure that is a cation ordered variant of the 6H hexagonal perovskite structure. The Sr-rich double perovskites undergo a cubic to tetragonal distortion upon cooling that is driven by out-of-phase octahedral tilting. The tetragonal distortion occurs upon cooling below 650 K in Sr_2NiOsO_6. The temperature of this transition decreases as the barium content increases and is completely suppressed for $x \geq 1.2$. All compositions in the double perovskite region become spin glasses below $T_g \approx 40$ K, due to the competition between ferromagnetic Ni–Os and antiferromagnetic Ni–Ni and Os–Os superexchange interactions. The double perovskite compositions that are rich in barium, like $Sr_{0.8}Ba_{1.2}NiOsO_6$ show some signs of magnetic ordering in small clusters, but the presence of Ba/Sr disorder inhibits long-range magnetic order. Trigonal Ba_2NiOsO_6 orders ferrimagnetically below $T_C = 108$ K. The magnetic structure of this compound contains ferromagnetic ~180° Ni–O–Os interactions and antiferromagnetic ~90° Ni–O–Os interactions, both in agreement with the Goodenough-Kanamori rules.

1. Introduction

The magnetic properties of A_2MOsO_6 double perovskites (A = Ca, Sr, Ba; M = Cr, Mn, Fe, Co, Ni, Cu) offer a fascinating yet perplexing glimpse into superexchange interactions between 3d and 5d transition metal ions. All A_2MOsO_6 double perovskites are semiconductors/insulators with magnetism that is determined by superexchange interactions between transition metal ions. Despite the structural and electronic similarities of these compounds they exhibit a diverse array of magnetic ground states including ferrimagnetic, noncolinear antiferromagnetic, metamagnetic, and spin glass states, as discussed in more detail below. The variety of magnetism that can be accessed in this family is a testament to the sensitivity of the exchange interactions to changes in the filling of the d-orbitals and/or distortions of the crystal structure.

Sr_2CrOsO_6 is a ferrimagnet with an antiparallel alignment of the spins on the Cr^{3+} ($t_{2g}^3e_g^0$) and Os^{5+} ($t_{2g}^3e_g^0$) ions, in agreement with the predictions of the Goodenough-Kanamori rules. It has an exceptionally high Curie temperature; Krockenberger et al. reported a T_C of 725 K [1], while Morrow et al. reported a somewhat lower value of 660 K [2]. The difference between the two is possibly related to differences in Cr/Os antisite disorder. Ca_2CrOsO_6 has a lower Curie temperature, $T_C = 490$ K, presumably due to a reduction in the strength of the Cr–O–Os superexchange interactions due to the increase in octahedral tilting [2]. A_2MnOsO_6 phases cannot be prepared under ambient pressure conditions, but Ca_2MnOsO_6 has been prepared using high pressure-high temperature conditions [3]. Like A_2CrOsO_6 compositions it is ferrimagnetic (T_C = 305 K), but understanding the superexchange interactions is complicated by the lack of long-range order between Mn^{3+} ($t_{2g}^3e_g^1$) and Os^{5+} ($t_{2g}^3e_g^0$) ions.

As filling of the 3d orbitals continues, ferrimagnetism gives way to antiferromagnetism in Sr_2FeOsO_6 and Sr_2CoOsO_6. In Sr_2FeOsO_6 the Goodenough-Kanamori rules [4] predict ferromagnetic coupling between Fe^{3+} ($t_{2g}^3e_g^2$) and Os^{5+} ($t_{2g}^3e_g^0$) ions, yet antiferromagnetic ordering is observed with one antiferromagnetic structure seen between 140 K and 67 K, and another below 67 K [5,6]. Ferromagnetism is also expected in Sr_2CoOsO_6, but here also two different antiferromagnetic structures are

* Corresponding author.
E-mail address: woodward.55@osu.edu (P.M. Woodward).

https://doi.org/10.1016/j.jssc.2022.123667
Received 27 July 2022; Received in revised form 1 October 2022; Accepted 10 October 2022
Available online 13 October 2022

observed. Below $T_{N1} = 108$ K antiferromagnetism driven largely by Os^{6+} ($t_{2g}^2e_g^0$) ordering is observed; further cooling leads to antiferromagnetic ordering of Co^{2+} ($t_{2g}^4e_g^2$) ions at $T_{N2} \approx 70$ K, leading to a noncolinear antiferromagnetic structure [7,8]. Ab initio calculations suggest that superexchange coupling between Co^{2+} and Os^{6+} is sufficiently weak that the two substructures effectively exhibit different ground states and spin dynamics [9]. Sr_2NiOsO_6 has been reported to be an antiferromagnet with $T_N = 50$ K, but no magnetic reflections were observed in low temperature powder neutron diffraction measurements, which leaves some open questions regarding its magnetic ground state [10]. A metastable high pressure form of Ba_2NiOsO_6 with the cubic double perovskite structure has been shown to be metamagnetic [11]. In the absence of an external magnetic field it orders with a modulated antiferromagnetic structure and a Néel temperature of 32 K, but application of an external field larger than 2.1 T results in a spin flop transition into a ferromagnetic state.

Somewhat surprisingly Ca_2FeOsO_6 ($T_C = 350$ K) [12], Ca_2CoOsO_6 ($T_C = 145$ K) [13], and Ca_2NiOsO_6 ($T_C = 175$ K) [10] are ferrimagnets, unlike their isoelectronic Sr_2MOsO_6 analogs. The antiparallel alignment of the 3d ion and osmium moments is a clear indication that antiferromagnetic M–O–Os exchange interactions are stronger than longer range M–M or Os–Os antiferromagnetic interactions. Not only do the M–O–Os interactions become stronger as the octahedral tilting increases—the M–O–Os bond angles decrease from 180° in the cubic structure to ~150° in Ca_2MOsO_6 phases—the antiferromagnetic nature of the coupling contradicts the predictions of the Goodenough-Kanamori rules. Using a combination of experiments and computations, Morrow et al. attribute this behavior to superexchange coupling between the M 3d e_g orbitals and the Os 5d t_{2g} orbitals [14]. The spatial overlap between these orbitals goes to zero as the bonds become linear, so this coupling is expected to weaken and eventually disappear as the tolerance factor [15] increases, which helps to explain why the magnetic ground state is so sensitive to structural distortions.

To better understand how changes in the crystal structure affect the various superexchange interactions in oxides containing both 3d and 5d transition metal ions we have investigated the $Sr_{2-x}Ba_xNiOsO_6$ phase diagram. With a $3d^8$ electron configuration the t_{2g} orbitals on Ni^{2+} are filled, leaving only the Ni e_g orbitals to participate in superexchange interactions. As the barium content increases the octahedral tilting distortions are reduced and finally suppressed entirely, before giving way to an entirely different topology in the trigonal structure of Ba_2NiOsO_6. This study provides an illuminating window into conditions where Goodenough-Kanamori rules are followed and the reasons why they are violated in double perovskites like Ca_2NiOsO_6. This paper is dedicated to both John Goodenough whose seminal work on magnetism inspired this study (and countless others) in celebration of his 100th birthday, and to Miguel Ángel Alario Franco who has inspired and supported so many of us through the years on the occasion of his 80th birthday.

2. Experimental

Polycrystalline samples of $Sr_{2-x}Ba_xNiOsO_6$ ($x = 0$–2) were synthesized using a conventional solid state method with stoichiometric amounts of BaO_2 (99%, Cerac), SrO_2 (99.9% trace metal basis, Sigma-Aldrich), NiO (99.9%, Strem Chemicals), and Os powder (99.9% trace metals basis, Sigma-Aldrich). The mixture was ground in a mortar and pestle and loaded in a capped alumina tube which was placed in a quartz tube along with a separate container of PbO_2. The quartz tube was sealed under vacuum and then heated to 1000 °C for 48 h. The PbO_2 acts as an in-situ oxygen source by decomposing to PbO and O_2 at ~600 °C. The quantity of PbO_2 was chosen to produce an excess of 1/4 mol O_2 to ensure complete oxidation to Os^{6+}. The stoichiometric reaction is shown below:

$$x\ BaO_2(s) + (2-x)\ SrO_2(s) + NiO(s) + Os(s) + (3/2)\ PbO_2(s) \rightarrow Sr_{2-x}Ba_xNiOsO_6(s) + (3/2)\ PbO(s) + (1/4)\ O_2(g)$$

The resulting black powders were then reground and reheated at 1100 °C for another 12 h to improve sample quality. Most samples had low levels (1–3% by mass) of unreacted NiO still present after the final reaction step.

Powder X-ray diffraction (PXRD) data was collected using a Bruker D8 Advance powder diffractometer (40 kV, 40 mA, sealed Cu X-ray tube) equipped with an incident beam monochromator (Johansson type SiO_2 crystal) and a Lynxeye XE-T position sensitive detector. Variable temperature X-ray diffraction data were collected on a Bruker D8 X-ray diffractometer equipped with a Lynxeye detector using Cu Kα radiation from a sealed tube. A Ni filter was used to remove Kβ radiation. For measurements above room temperature the sample was heated in air using an Anton-Paar htk1200 furnace. For measurements below room-temperature, data was collected in reflection geometry from 10 K to 300 K with 5 K steps using an Oxford Cryosystems pHeniX cryostat. Phase purity and cation ordering were determined by the Rietveld refinements as implemented in TOPAS-Academic (v6).

Neutron powder diffraction (NPD) measurements for the $x = 0.6$ sample were conducted at the POWGEN beamline at the Spallation Neutron Source at Oak Ridge National Laboratory. A 1.2 g sample of $Sr_{1.4}Ba_{0.6}NiOsO_6$ was loaded into a 6 mm vanadium can and mounted in the POWGEN Automatic Changer (PAC). At both 10 K and 60 K a 1 h scan was taken at 1.066 Å, and a 2 h scan was taken at 3.731 Å. At 300 K a 2 h scan was taken at 1.066 Å, and a 1 h scan at 3.731 Å.

Additional NPD measurements were conducted at the GEM (General Materials Diffractometer) instrument at the ISIS neutron and muon source on the $x = 1.2$ and 2.0 samples. Approximately 7 g of each composition was made by combining six samples, each ~1 g in mass. After the samples were combined, they were heated once more in an evacuated quartz tube at 1000 °C for 24 h to insure homogenization. For the $x = 1.2$ sample, 1 h scans were collected at 300 K, 200 K, 150 K, 120 K, 100 K, 90 K, 75 K, 60 K, and 50 K; 2 h scans were collected at 40 K, 25 K, and 10 K; and a 4 h scan was collected at 5 K. For the x = 2.0 sample, 1 h scans were collected at 300 K, 200 K, 150 K, 120 K, 90 K, 75 K, 60 K, 50 K, 25 K, and a 2 h scan was collected at 5 K. Rietveld refinements against the NPD data were carried out using both TOPAS-Academic (v6) [16] and GSAS [17].

DC magnetic susceptibility was measured as a function of temperature between 400 K and 2.5 K with an applied field of 1000 Oe in zero field cooled (ZFC) and field cooled (FC) conditions using a Superconducting Quantum Interference Device (SQUID). For each measurement a 30–40 mg sample was loaded in a gelatin capsule and mounted in a plastic straw. The diamagnetic contribution from core electrons was subtracted prior to analyzing the data. Magnetization versus applied field data were taken on the same instrument with an applied field of −70 kOe to +70 kOe at 5 K and 300 K for all samples, and also at 60 K for the $x =$ 1.4, 1.6, 1.8, and 2.0 samples.

AC magnetic susceptibility measurements were obtained for the $x =$ 0.6 and 1.2 samples using a Quantum Design Physical Property Measurement System (PPMS). For each composition the same sample was used for the PPMS and SQUID measurements. The experiment spanned the range of 50–10000 Hz and 20–60 K with a magnetic field of 0.02 Oe. Heat capacity was collected for the $x = 1.2$ sample from 20 K to 300 K with step size of 4 K on the PPMS.

3. Results

3.1. Crystal structure

The room temperature PXRD patterns for $Sr_{2-x}Ba_xNiOsO_6$ were modeled with one of three different structural modifications: an undistorted cubic double perovskite structure (space group $Fm\bar{3}m$), a tetragonal distortion of this structure brought about by out-of-phase tilting of the octahedra about the *c*-axis (space group $I4/m$), or a trigonal 6L perovskite structure which contains both corner- and face-sharing

octahedra (space group $P\bar{3}m1$). The latter structure is closely related to the more familiar 6H hexagonal perovskite but ordering of Ni and Os cations lowers the symmetry from hexagonal to trigonal. All PXRD refinements were completed assuming a random distribution of Ba^{2+} and Sr^{2+} ions at the *A*-site. The possibility of antisite disorder between Ni^{2+} and Os^{6+} cations was investigated, but the introduction of antisite disorder did not improve the quality of the fits to the PXRD data sets. Therefore, complete ordering of the B-site cations was assumed in the neutron diffraction refinements, which are less sensitive to antisite disorder due to the similar neutron scattering lengths of osmium (b_{coh} = 10.7 fm) and nickel (b_{coh} = 10.3 fm).

PXRD patterns of the $x = 0.0$–0.6 samples were fitted with the $I4/m$ model previously reported for Sr_2NiOsO_6 [10]. Peak splitting indicative of the tetragonal distortion cannot clearly be discerned for the $x = 0.6$ sample, though a slightly asymmetric peak profile suggests the symmetry is lower than cubic. The room temperature PXRD pattern of the $x = 0.6$ sample was fitted with both $I4/m$ and $Fm\bar{3}m$ models, with the tetragonal structure giving a better fit (R_{wp} = 11.54% vs R_{wp} = 13.23%). It has previously been shown that superstructure peaks originating from rock salt ordering of the octahedral site cations can obscure superstructure peaks that arise from out-of-phase tilts of the octahedra [18]. The scattering power of the oxygen atoms relative to the heavier cations is much larger for neutrons than it is for X-rays, which makes NPD the preferred technique for identifying subtle octahedral tilting distortions. For the $x = 0.6$ sample the cubic $Fm\bar{3}m$ model does not properly account for the intensities of several weak superstructure reflections with odd-odd-odd Miller indices, as shown in Fig. 2. Fitting with the $I4/m$ space group improves the fit of these low intensity reflections, dropping the R_{wp} from 7.02% to 6.64%. The reduction in symmetry allows for distortions and rotations of the octahedra. The octahedral rotations bend the Ni–O(2)–Os bond angles in the ab-plane, which would be linear in the cubic structure, to a value of 173.2(5)° at 300 K. Crystallographic data for $Sr_{1.4}Ba_{0.6}NiOsO_6$ are given in the supporting information.

The room temperature PXRD pattern of the $x = 0.8$–1.2 samples can be satisfactorily fit with the cubic $Fm\bar{3}m$ structural model. This model accounts for all peaks in both X-ray and neutron diffraction patterns of the $x = 1.2$ sample. Variable temperature NPD data shows that the cubic symmetry observed at room temperature is maintained down to at least 5 K. The Os–O and Ni–O bond distances are 1.9268(5) Å and 2.0581(5) Å, respectively, at room temperature. Full details of the crystal structure and the temperature evolution of the cubic lattice parameter can be found in the supporting information.

The PXRD patterns of the $x = 1.4$–1.8 samples show a mixture of the $Fm\bar{3}m$ and $P\bar{3}m1$ phases with the phase fraction of the trigonal phase increasing as the barium content increases (see Tables S3 and S5 in the supporting information). In the PXRD pattern of Ba_2NiOsO_6 the peaks assigned to the cubic $Fm\bar{3}m$ structure are no longer observed. The phase fractions obtained from Rietveld refinements were used in conjunction with the lever rule to estimate the width of the two-phase region. Using phase fractions obtained from the PXRD patterns of the $x = 1.4$, 1.6, and 1.8 samples the two-phase region is estimated to extend from x = 1.35(1) to x = 1.83(1).

Three different models were investigated to describe the crystal structure of Ba_2NiOsO_6. All three have the connectivity of the 6H perovskite structure, featuring both dimers of face sharing octahedra and octahedra that are connected to their neighbors exclusively through shared corners (see Fig. 1c). In the $P6_3/mmc$ model, there is one site for the cations that occupy the face sharing octahedra and another for the cations that reside in the octahedra that share only corners. This is the structure adopted by ternary AMO_3 6H perovskites, as well as $Ba_3Mn_2OsO_9$ [19] and $Ba_3Fe_2TeO_9$ [20], where the lower valent 3d transition metal ion preferentially occupies the octahedra that share faces. In the $P6_3mc$ model, the cation sites within the face-sharing octahedral dimers become inequivalent, facilitating cation ordering within those dimers. This structure has been reported for $Ba_2Fe_{0.86}Os_{1.14}O_6$ ($Ba_3Fe_{1.3}Os_{1.7}O_9$) and $Ba_2Co_{0.84}Os_{1.16}O_6$ ($Ba_3Fe_{1.26}Os_{1.74}O_9$).[18] If cation ordering occurs in both the face-sharing and corner-sharing octahedra, as reported for $Ba_2Fe_{1.12}Os_{0.88}O_6$ ($Ba_3Fe_{1.68}Os_{1.32}O_9$), the symmetry is further lowered to $P\bar{3}m1$ [21]. Because all three structures have similar unit cell dimensions, an analysis of the systematic absences is the best way to differentiate between them.

Rietveld refinements against the Ba_2NiOsO_6 PXRD pattern show that the $P\bar{3}m1$ space group yields the best fit, as shown in Fig. 3. This finding is in agreement with a previous report of the crystal structure of Ba_2NiOsO_6 [22]. Refinements of site occupancies show that the Ni^{2+} and Os^{6+} cations are ordered so that each face-sharing dimer contains one nickel and

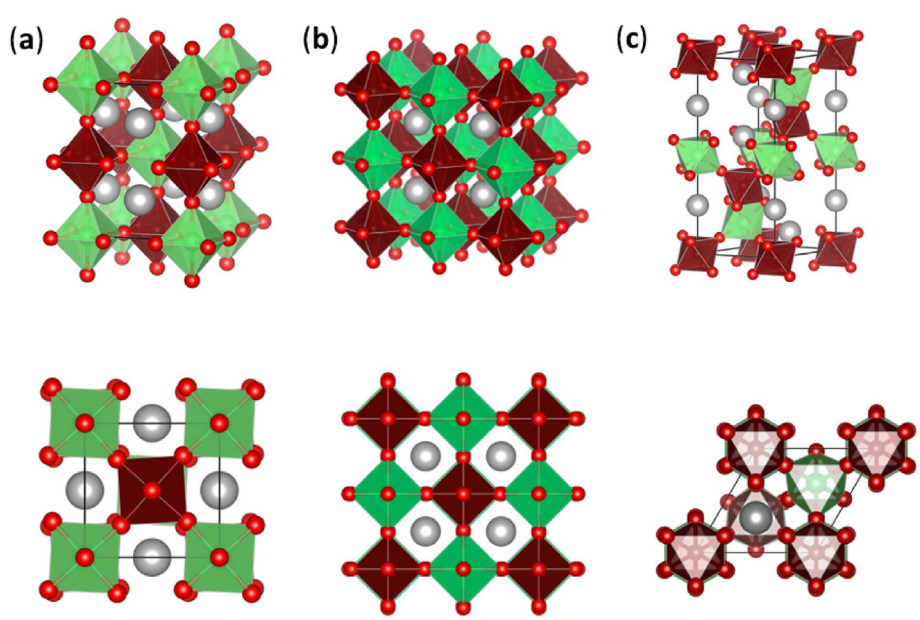

Fig. 1. The structures observed in the $Sr_{2-x}Ba_xNiOsO_6$ phase diagram: (a) a tetragonally distorted double perovskite structure with $I4/m$ symmetry, (b) a cubic double perovskite structure with $Fm\bar{3}m$ symmetry, and (c) a trigonal 6L ordered "hexagonal perovskite" structure with $P\bar{3}m1$ symmetry. The Ni- and Os-centered octahedra are shown in green and maroon, respectively. The Sr/Ba ions are shown in silver and the oxide ions in red.

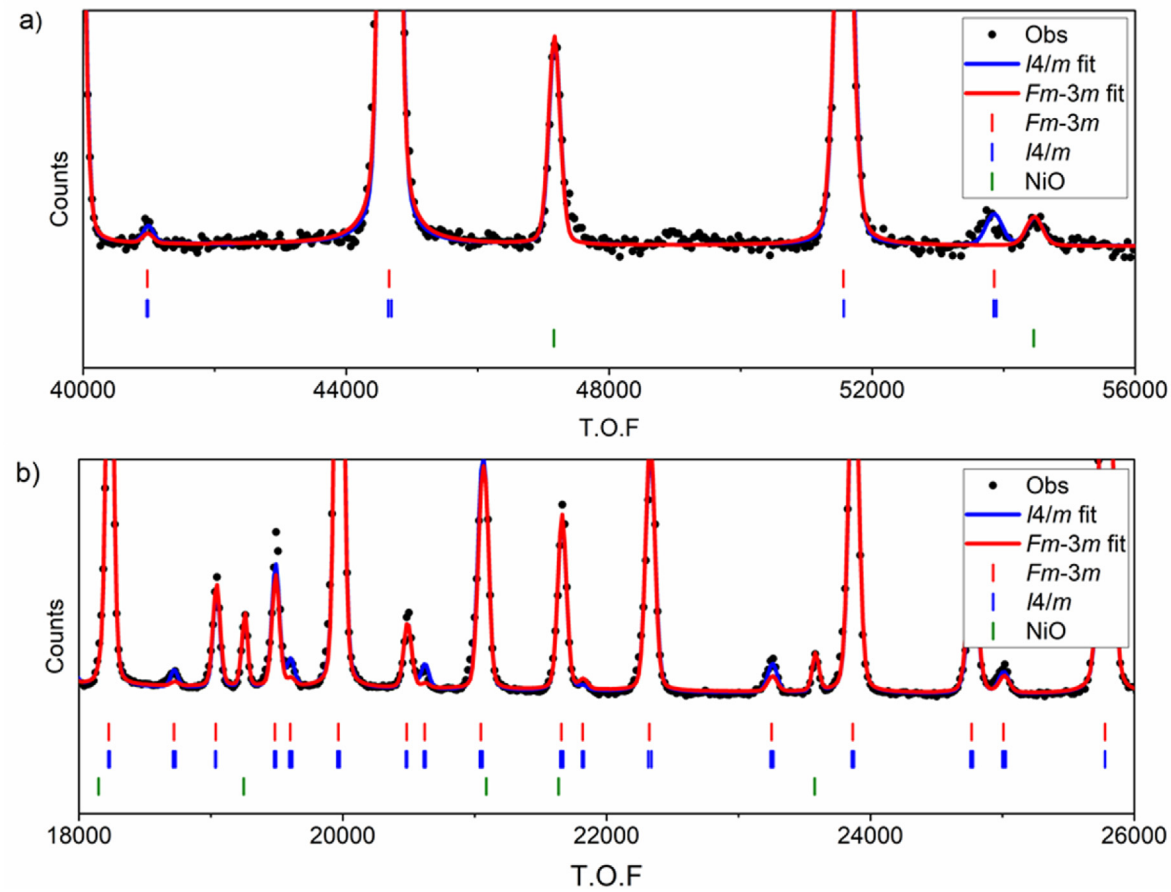

Fig. 2. Fits to the powder neutron diffraction pattern of the $Sr_{1.4}Ba_{0.6}NiOsO_6$ ($x = 0.6$) sample collected at 300 K. The *I4/m* structural model shown in blue gives a fit that is superior to the cubic $Fm\bar{3}m$ model. The NiO content is 2.4% by mass.

one osmium cation. Ordering of the cations over the corner-sharing octahedral sites occurs so that each oxygen makes one bond to Ni^{2+} and one bond to Os^{6+}, as found in the double perovskite structure of Sr_2NiOsO_6.

Rietveld refinements against the Ba_2NiOsO_6 neutron powder pattern were carried out to accurately determine key bond distances and angles. The osmium and nickel cations that reside in octahedra that only share corners have Os–O distances of 1.933(1) Å (× 6) and Ni–O distances of 2.070(1) Å (× 6), respectively. The cations that sit in the octahedra that share a common face are displaced away from one another, presumably due to electrostatic repulsions between Ni^{2+} and Os^{6+}. Consequently, the metal-oxygen distances to the oxygens in the shared face are longer than those to the opposite face of the octahedron. The Os–O bonds are 1.959(2) Å (× 3) and 1.938(1) Å (× 3), while the Ni–O bonds are 2.079(2) Å (× 3) and 2.001(1) Å (× 3). The Os–O–Ni bond angle across the shared corner is linear within experimental error, 179.95(8)°, while the Os–O–Ni angle involving the oxygens in the shared face is 82.73(4)°. The observation that the latter angle is < 90° would also be consistent with a structural response that attempts to minimize electrostatic repulsions between cations across the shared face.

3.2. Sr_2NiOsO_6–Ba_2NiOsO_6 phase diagram

Octahedral tilting distortions in perovskites, like the one that lowers the symmetry from cubic to tetragonal, occur because one or more rotational phonon modes freeze out. At high temperatures the octahedral tilts are dynamic, increasing the symmetry of the time-averaged structure, while at low temperatures a cooperative tilting distortion occurs. High temperatures favor the cubic $Fm\bar{3}m$ structure, whereas lower temperatures favor the tetragonal *I4/m* structure. The temperature of the cubic to tetragonal phase transition is expected to increase as the tolerance factor decreases. Variable temperature diffraction data was collected on several Sr-rich samples to assess the temperatures at which this phase transition occurs.

Fig. 4 shows the temperature dependent evolution of the lattice parameters for the $x = 0$, 0.2, and 0.4 samples, as determined from analysis of PXRD data. The *a* lattice parameter of the tetragonal structure (a_t) is related to the *a* lattice parameter of the cubic structure (a_c) by the relationship $a_t\sqrt{2} \approx a_c$. Thus, the tetragonal to cubic phase transition is expected to occur near the temperature where $a_t\sqrt{2}$ and c_t converge. This occurs near 650 K for $Sr_2NiOsO6$, 530 K for $Sr_{1.8}Ba_{0.2}NiOsO_6$, and 450 K for $Sr_{1.6}Ba_{0.4}NiOsO_6$.

The temperature dependent evolution of the lattice parameters for the $x = 1.2$ and 1.4 samples are shown upon lowering the temperature from room temperature in the supporting information. A contraction of the cubic unit cell parameter is seen in both samples, but no transition from cubic to tetragonal can be seen in either sample. The x = 1.4 contains a mixture of cubic and 6L trigonal phases. The refinements show no change in the phase fractions of the two phases as a function of temperature. Variable temperature NPD analysis of Ba_2NiOsO_6 shows a smooth evolution of the unit cell parameters as a function of temperature (see supporting information, Fig. S4), indicating that no structural phase transition occurs below room temperature.

Using the diffraction data described above, the phase diagram for the Sr_2NiOsO_6–Ba_2NiOsO_6 system can be derived and is shown in Fig. 5. The exact temperature of the cubic to tetragonal phase transition for the x = 0.6, 0.8, and 1.0 samples is not definitively known, so a linear extrapolation of the phase transition temperature has been made from the more

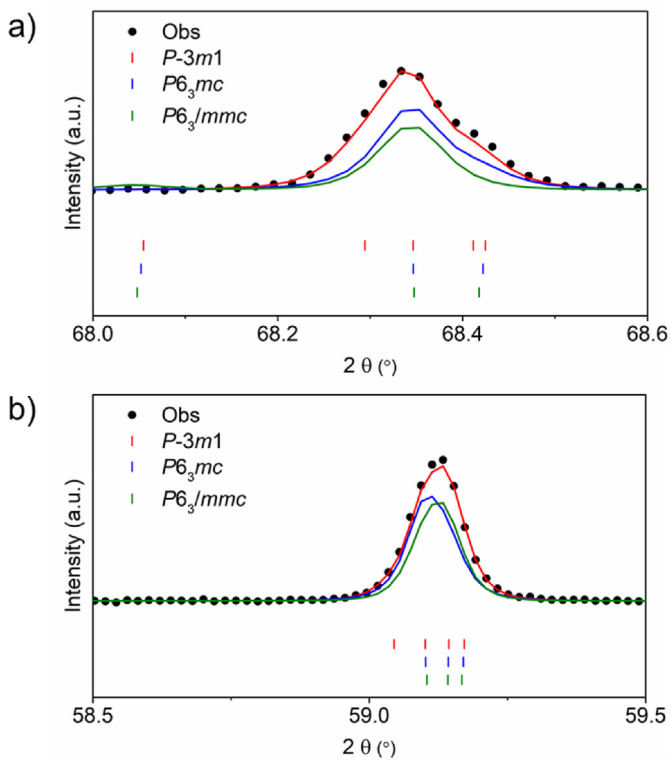

Fig. 3. A comparison showing the calculated fit to selected peaks in the PXRD pattern of Ba_2NiOsO_6 using structural models with $P\bar{3}m1$, $P6_3mc$, and $P6_3/mmc$ space group symmetry.

Sr-rich samples. This extrapolation predicts that $Sr_{1.4}Ba_{0.6}NiOsO_6$ is tetragonal at room temperature and $Sr_{0.8}Ba_{1.2}NiOsO_6$ is cubic at 5 K, both of which are consistent with the diffraction data already discussed.

The unit cell volume divided by the number of formula units per unit cell is plotted in Fig. 5b. Not only does the unit cell volume expand as strontium is replaced by the larger barium, the trigonal 6L phase has a volume that is approximately 5% larger than the cubic phase for those samples where both phases are present in equilibrium. Even if one extrapolates the volume of the single-phase cubic region across to the Ba_2NiOsO_6 composition, the cubic phase would be significantly smaller in volume than the trigonal phase. This explains why high-pressure synthesis can be used to prepare a metastable cubic form of Ba_2NiOsO_6 [11].

3.3. Magnetic properties

The DC magnetic susceptibility data as a function of temperature for $Sr_{2-x}Ba_xNiOsO_6$ samples from $x = 0.2$ to 1.2 are shown in Fig. 6a. All six samples show very similar magnetism, with an antiferromagnetic-like cusp near 40 K and a divergence between the field cooled and zero-field cooled curves below this cusp. Isothermal magnetization at 5 K is linear for the $x = 0.2$ sample, but as the amount of barium substitution increases a small opening is observed that does not saturate up to 70 kOe (Fig. 6c). Variable temperature DC magnetic susceptibility data for the single phase trigonal Ba_2NiOsO_6 sample ($x = 2$) shows a ferromagnetic-like transition at 108 K where a sharp rise in magnetic susceptibility occurs. Isothermal magnetization shows a magnetic hysteresis with a saturation magnetization of 0.51 μ_B/f.u and 0.71 μ_B/f.u at 60 K and 5 K, respectively. The magnitude of the saturation magnetization suggests that ferrimagnetism is more likely than ferromagnetism.

DC magnetic susceptibility of the x = 1.4–1.8 samples, which are a mixture of cubic and trigonal phases, show features consistent with both phases. The presence of a ferrimagnetic trigonal phase leads to a sharp rise in susceptibility near 108 K. The height of the rise in magnetization below the Curie temperature increases as the phase fraction of the trigonal phase increases. The $x = 1.4$ and 1.6 samples with ~10% and ~50% trigonal phase also show a weak cusp at approximately 40 K, which presumably originates from the cubic $Fm\bar{3}m$ phase. The isothermal magnetization measurements reveal an opening that does not saturate.

The cusp seen in the temperature-dependent susceptibility plots for the cubic and tetragonal double perovskite compositions ($0 < x \leq 1.2$) is suggestive of antiferromagnetic ordering. However, the FC–ZFC divergence as well as the opening of a loop in the isothermal magnetization curves imply that the ground state may be a spin glass. To investigate this possibility the AC magnetic susceptibilities of the $x = 0.6$ and 1.2 samples were measured (Fig. 7). The susceptibility maximum for the $x = 0.6$

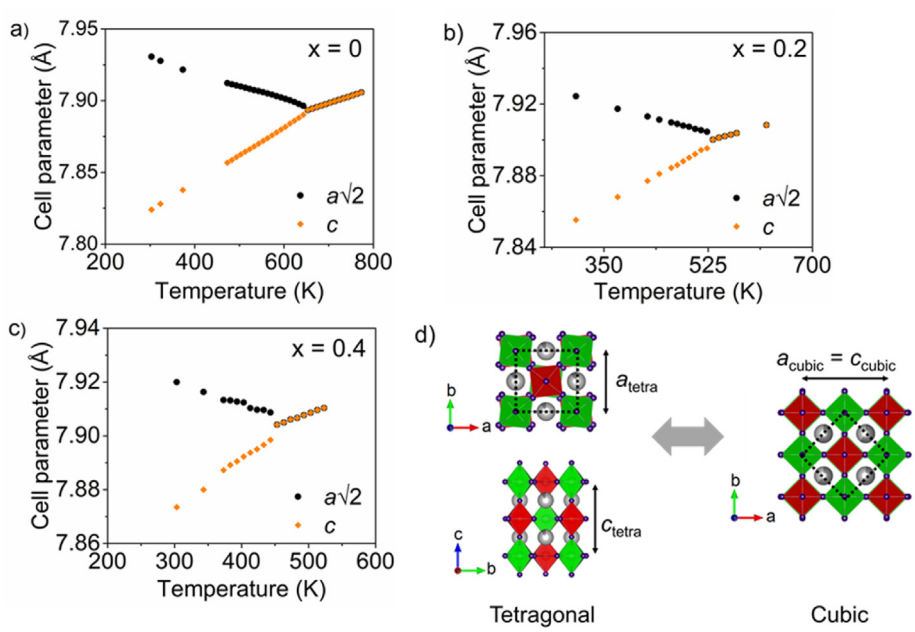

Fig. 4. Cell parameters for several $Sr_{2-x}Ba_xNiOsO_6$ samples as a function of temperature: (a) $x = 0$, (b) $x = 0.2$, (c) $x = 0.4$. (d) The relationship between the tetragonal and cubic unit cells.

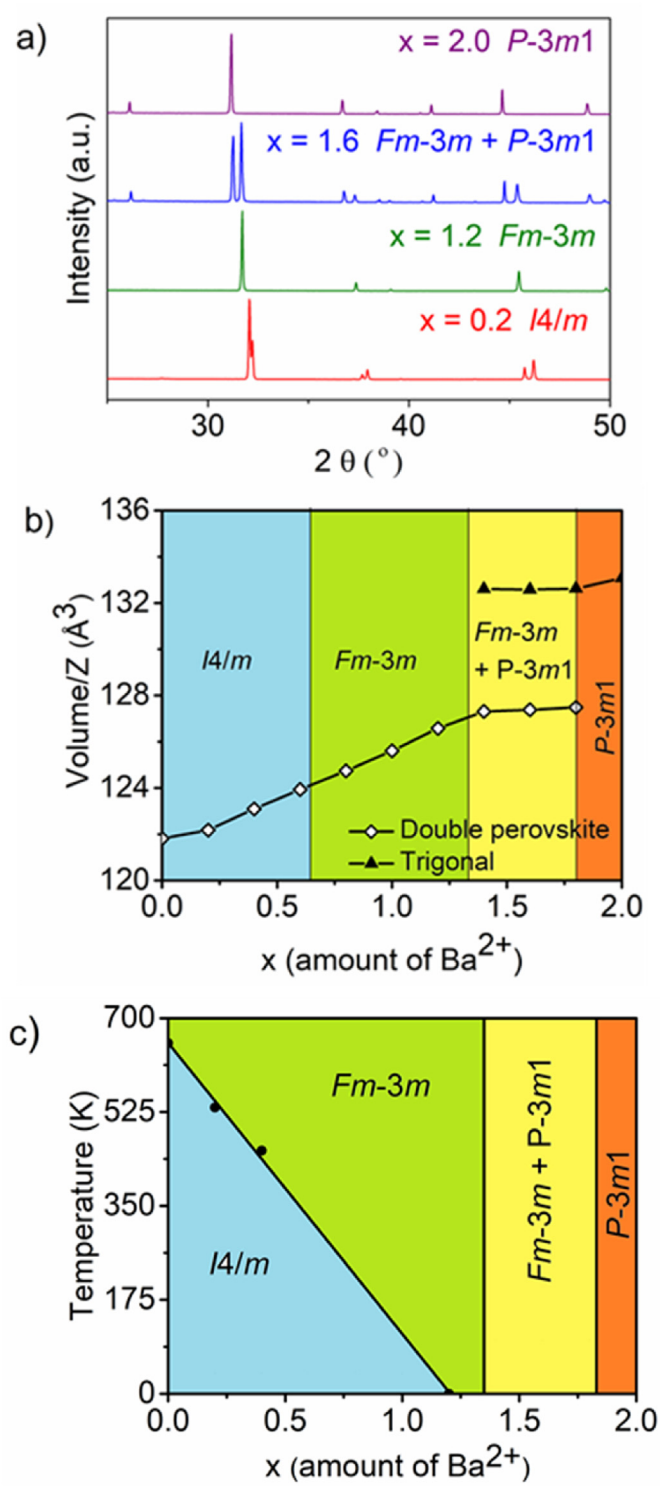

Fig. 5. (a) PXRD patterns of the four structural regions for the $Sr_{2-x}Ba_xNiOsO_6$ system, (b) volume/Z at room temperature as a function of the barium content, (c) structural phase diagram.

sample shows a slight shifting to higher temperatures with increasing frequency, consistent with a glassy magnetic ground state [6]. For the x = 1.2 sample, typical glassy frequency dependence of the transition temperature was not observable in the AC susceptibility measurement within the 1 K step size used for the data collection, however, the lack of an anomaly in specific heat measurements on the $x = 1.2$ sample (Fig. 8) would seem to rule out long-range antiferromagnetic order.

Weiss temperatures and effective moments extracted from Curie-Weiss plots are given in Table 1. For the cubic and tetragonal phases the Weiss constants are all positive suggesting that ferromagnetic interactions are dominant. The Weiss constant steadily increases as the Ba-content increases, despite the fact that the glass transition temperature does not shift appreciably with composition. The effective moment values are close to ~3.6 μ_B regardless of the barium content. The spin-only moments for a d^2 Os^{6+} ion and a d^8 Ni^{2+} ion are both 2.83 μ_B, and if one assumes a negligible interaction between the two ions the spin-only effective moment would be $[(2.83\ \mu_B)^2 + [(2.83\ \mu_B)^2]^{1/2} = 4.00\ \mu_B$. That the observed μ_{eff} is smaller than 4 μ_B indicates that spin-orbit coupling (SOC) effects are larger for osmium with a 5 d^2 configuration, where SOC reduces the moment, than for nickel with a 3 d^8 configuration where SOC should increase the effective moment. The fact that T_C of Ba_2NiOsO_6 is six times larger than the absolute value of θ_{CW} (108 K vs −18 K) indicates that both antiferromagnetic and ferromagnetic interactions are present, but they are not necessarily competing against one another. The negative Weiss constant indicates that antiferromagnetic interactions are stronger than ferromagnetic interactions.

3.4. Magnetic structure

To look for signatures of long-range magnetic ordering, neutron diffraction data for the $x = 0.6$ sample was taken above and below the 40 K cusp observed in the magnetic susceptibility data. Comparing the neutron diffraction patterns collected at 60 K and 10 K shows neither a noticeable change in the intensity of any reflection nor the presence of new reflections. This confirms the earlier conclusion that the tetragonal *I4/m* compositions do not exhibit long range magnetic order, but instead adopt a spin glass state below 40 K.

The magnetization of the $Sr_{0.8}Ba_{1.2}NiOsO_6$ ($x = 1.2$) sample is similar to the x = 0.6 sample, but the crystal structure remains cubic down to at least 5 K. Variable temperature neutron diffraction taken for the $x = 1.2$ sample above and below 40 K show weak signatures of magnetic ordering. The neutron diffraction pattern collected at 10 K, 25 K, and 60 K are subtracted from the pattern collected at 5 K in Fig. 8. The difference pattern shows the emergence of two broad and weak features at d-spacings of 4.44 Å and 4.27 Å. The metastable cubic double perovskite form of Ba_2NiOsO_6 prepared at high pressure, orders with a modulated antiferromagnetic ground state below 32 K, and its strongest magnetic reflections are at ~4.44 Å and ~4.27 Å [11]. The weak and broad magnetic features seen in the x = 1.2 sample are consistent with what would be expected if cubic $Sr_{0.8}Ba_{0.8}NiOsO_6$ underwent the same ordering. However, the lack of a discernible anomaly in the specific heat data, taken together with the very weak and broad peaks seen in the neutron data, suggest that the magnetic ordering in the former is short-range at best, presumably due to the disordered arrangement of barium and strontium ions.

Variable temperature neutron diffraction patterns of Ba_2NiOsO_6 (x = 2.0) reveal changes in the intensity of reflections such as $(2\bar{1}1)$ and $(10\bar{3})$ below the Curie temperature of 108 K (Fig. 9). A Pawley fit of the neutron diffraction data at 5 K in the $P\bar{3}m1$ space group accounts for all reflections, indicating that the magnetic unit cell is identical to the nuclear unit cell. Using ISODISTORT [23], the magnetic structures consistent with k point (000) were generated. Possible magnetic space groups are $P\bar{3}m'1$, $C2/m$, $C2'/m'$, $P\bar{1}$, $P\bar{3}'m'1$, $C2'/m$, $C2/m'$, and $P\bar{1}'$. Rietveld refinements with comparable goodness of fit and R_{wp} can be obtained in each of these space groups. However, the $C2/m$, $C2'/m'$, $C2'/m$, and $C2/m'$ space groups all predict reflections that are not observed in the neutron diffraction pattern, and therefore were rejected. Placing the constraint that all Ni sites have moments equal in magnitude to one another, and the same constraint on Os, suggests either $P\bar{3}m'1$ or $P\bar{1}$ space groups as the best choices. Since there is no meaningful improvement in the refinement in the lower symmetry $P\bar{1}$, we describe the magnetic structure of Ba_2NiOsO_6 with the magnetic space group $P\bar{3}m'1$. The Ni and

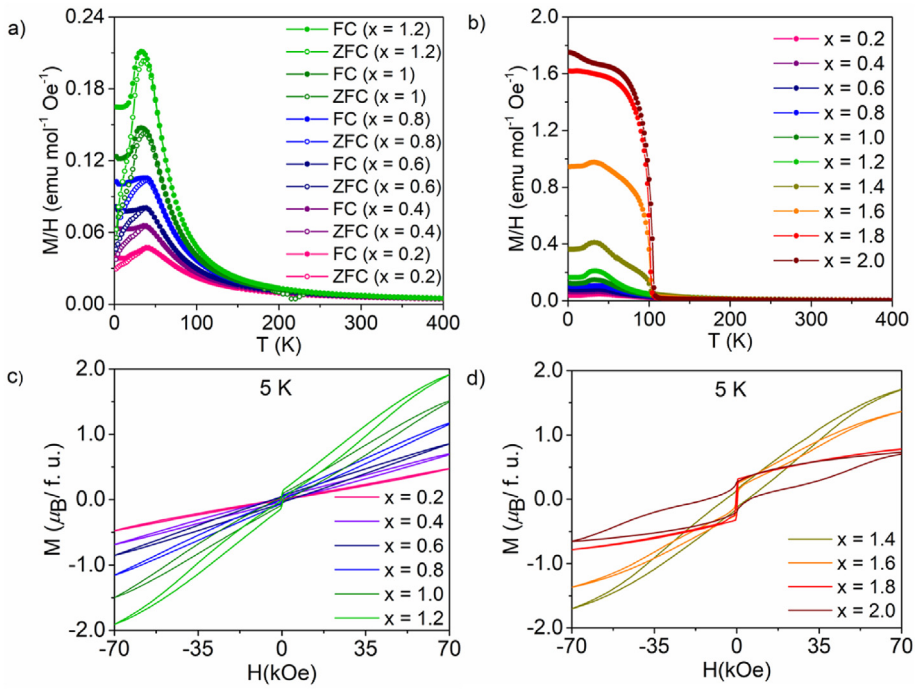

Fig. 6. (a) Field cooled and zero field cooled magnetic susceptibility of $Sr_{2-x}Ba_xNiOsO_6$ samples with $x = 0.2$–1.2 as a function of temperature. (b) Field cooled magnetic susceptibility for all samples studied. (c) Isothermal magnetization at 5 K for samples with x = 0.2–1.2. (d) Isothermal magnetization at 5 K for samples with x = 1.4–2.0.

Os ions that share a common octahedral face couple antiferromagnetically, while the ions that are linked via corner-connected octahedra couple ferromagnetically, as shown in Fig. 9. This confirms the ferrimagnetic structure expected from the magnetization measurements.

The magnetic moments refine to 1.47(2) μ_B for Ni^{2+} and 0.34(4) μ_B for Os^{6+} at 5 K. Every magnetic unit cell contains three formula units, so the calculated magnetization per unit cell is $|Ni(1) - 2 \times (Ni(2)) - Os(1) + 2 \times (Os(2))| = 1.13\ \mu_B$ at 5 K. Dividing by the number of formula unit per unit cell gives 0.38 μ_B/f.u. at 5 K. The net magnetization estimated from these moments is about half the saturated moment of 0.71 μ_B/f.u. obtained from isothermal magnetization measurements. Delocalization of spin density to the oxide ions, which is not detected in neutron diffraction, is one possible source of the discrepancy.

In previous studies a combination of spin orbit coupling and covalency with oxygen has been invoked to explain the reduction in the size of the 5d [2] Os^{6+} magnetic moment from the 2 μ_B spin-only value expected in the strong field limit appropriate for a magnetically ordered state. Experimentally, this moment as been reported as high as 0.60 μ_B in Sr_2MgOsO_6 at 10 K, or as low as 0.2–0.3 μ_B at 3–4 K in Ba_2CaOsO_6, Ba_2MgOsO_6, Ba_2ZnOsO_6 [8–10]. The magnetic moments reported for Ni^{2+} obtained at 2 K have been reported as 1.92(6) μ_B and 2.04(6) μ_B for Sr_2NiMoO_6 and Ba_2NiMoO_6 respectively [24]. Therefore, the refined magnetic moments we obtain for these two ions in Ba_2NiOsO_6 are in the expected range for Os^{6+} and somewhat smaller than expected for Ni^{2+}.

4. Discussion

The Goodenough-Kamamori rules for 180° superexchange between Ni^{2+} and Os^{6+} ions predict ferromagnetic coupling. Based on that prediction, a cubic double perovskite with an ordered array of these two ions on the octahedral sites should be ferromagnetic. Instead, the high-pressure form of Ba_2NiOsO_6, which adopts the cubic double perovskite structure, has a modulated antiferromagnetic ground state that is 8 unit cells in length along one crystallographic axis. The ferromagnetic state can only be accessed with an external applied field of 2.1 T [3]. The complex magnetic structure and behavior indicates the presence of competing antiferromagnetic interactions. While local Ni–O–Os interactions in this magnetic structure appear to be ferromagnetic, the competition from the longer-range antiferromagnetic Ni–Ni and Os–Os superexchange interactions results in a modulated antiferromagnetic structure.

For all samples with the double perovskite structure, either with *I4/m* or $Fm\overline{3}m$ symmetry, a cusp at 40 K is observed in the magnetic susceptibility data. Neutron diffraction of the $x = 0.6$ sample with the *I4/m* structure at 60 K and 10 K showed no signature of magnetic ordering, and ac susceptibility measurements show a frequency dependent shift of the cusp, both of which suggest a glassy transition. Previous literature on tetragonal *I4/m* Sr_2NiOsO_6 with neutron diffraction data at 10 K also failed to observe magnetic reflections [10]. While the magnetic ground state was previously thought to be antiferromagnetic, the data presented here suggests that a spin glass state is a more appropriate assignment.

The high-pressure cubic form of Ba_2NiOsO_6 and the $Ba_{1.2}Sr_{0.8}NiOsO_6$ sample studied here are isostructural but their magnetic properties are different. The Os–O distances for the two compounds, 1.9268(5) Å for $Ba_{1.2}Sr_{0.8}NiOsO_6$ and 1.927(2) Å for Ba_2NiOsO_6, are equivalent within experimental error, and the Ni–O distances are elongated from 2.0581(5) Å in $Ba_{1.2}Sr_{0.8}NiOsO_6$ to 2.088(2) Å in Ba_2NiOsO_6. Given the structural similarities it would appear the antiferromagnetic ground state and metamagnetic transitions of cubic Ba_2NiOsO_6 are sensitive to local distortions that arise from Sr/Ba disorder. Long range antiferromagnetic Ni–Ni and Os–Os superexchange interactions compete with ferromagnetic Ni–O–Os interactions, and the relative strengths of these interactions are sensitive to changes in bond angles. While the average structure of $Ba_{1.2}Sr_{0.8}NiOsO_6$ is cubic, locally there will be a random mix of close-to-linear Ni–O–Os bonds and bent Ni–O–Os bonds due to the Sr/Ba disorder. The presence of weak signatures of magnetic scattering in neutron powder diffraction patterns of $Ba_{1.2}Sr_{0.8}NiOsO_6$ suggests that small clusters of the modulated antiferromagnetic structure form, but the Sr/Ba disorder disrupts long-range coherence of this magnetic structure.

When synthesized at ambient pressures the structure of Ba_2NiOsO_6 consists of alternating layers of Ni and Os octahedra that are corner connected, and face-sharing octahedral dimers, where each dimer

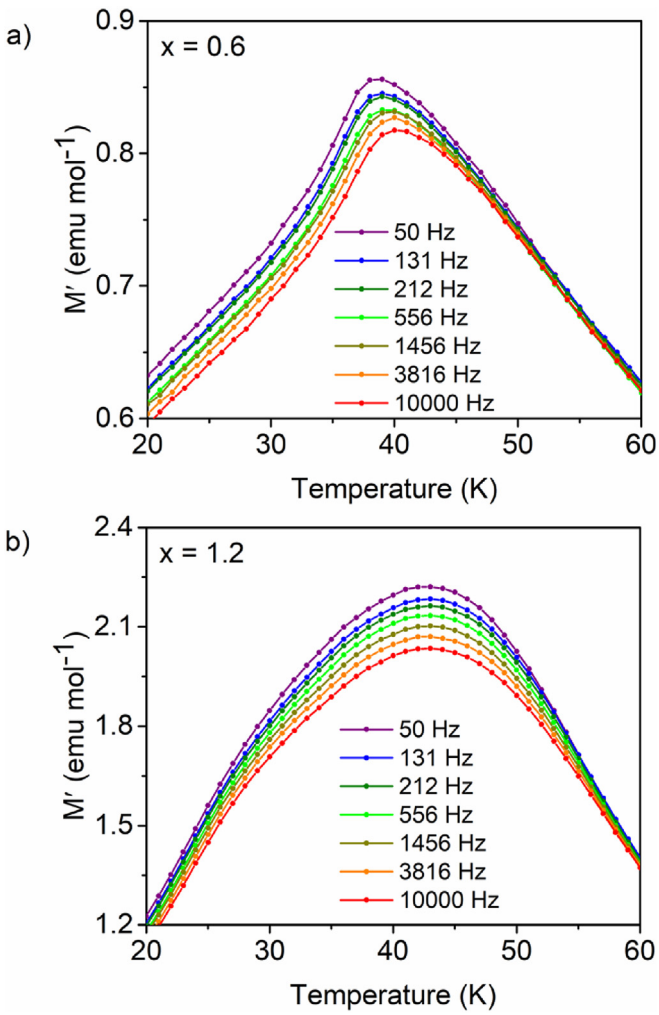

Fig. 7. AC magnetic susceptibility for the x = 0.6 and x = 1.2 samples.

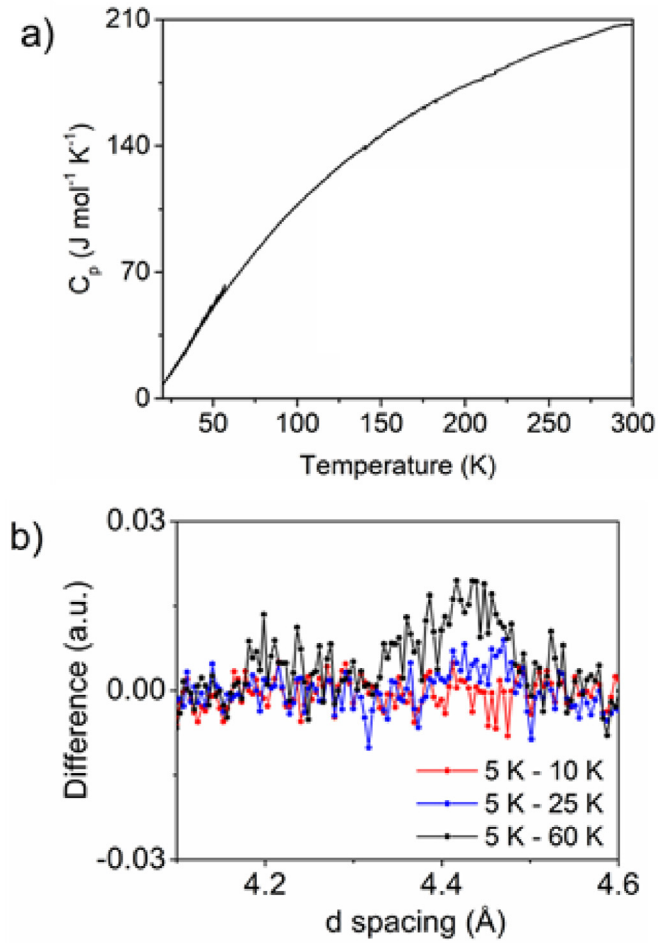

Fig. 8. (a) Specific heat measurement for x = 1.2 sample. No feature is observed around 40 K which suggests the cusp in the magnetic susceptibility data is not associated with a transition to a long range ordered state. (b) The difference between the 5 K pattern and the 10 K, 25 K, and 60 K patterns for $Ba_{1.2}Sr_{0.8}NiOsO_6$.

contains one Ni^{2+} and one Os^{6+}. Both magnetization and neutron powder diffraction experiments indicate that trigonal Ba_2NiOsO_6 has a ferrimagnetic ground state. From the magnetic structure we see that Ni- and Os-centered octahedra that share corners couple ferromagnetically, while those that share faces couple antiferromagnetically. Both interactions are consistent with the Goodenough-Kanamori rules for 180° and 90° superexchange. It would appear that the topology of the trigonal structure diminishes the importance of the longer range Ni–Ni and Os–Os antiferromagnetic interactions such that the shorter range Ni–O–Os superexchange interactions are dominant.

5. Conclusions

The crystal chemistry and magnetism of compositions in the $Sr_{2-x}Ba_xNiOsO_6$ phase diagram have been investigated. Samples with $x < 1.35$ adopt a double perovskite structure, while samples with $x > 1.83$ adopt a trigonal structure that is a cation ordered variant of the 6H hexagonal perovskite structure. The two regions are separated by a miscibility gap. The Sr-rich double perovskites undergo a cubic to tetragonal distortion upon cooling that is driven by out-of-phase octahedral tilting. The phase transition temperature decreases as the Ba content and tolerance factor increase. For samples with x ≥ 1.2 the cubic structure is retained down to at least 5 K.

Compositions with a tetragonally distorted double perovskite structure are spin glasses below 40 K due to the competition between ferromagnetic Ni–O–Os nearest neighbor interactions and longer range antiferromagnetic Ni–Ni and Os–Os superexchange interactions. These phases have positive Weiss constants confirming the presence of ferromagnetic Ni–O–Os coupling. In the compositions that retain the cubic structure to low temperature, long range magnetic order is inhibited by Sr/Ba disorder, but very weak magnetic scattering intensity can be seen in the neutron powder diffraction data that suggests the formation of short-range ordered clusters.

Table 1
Weiss temperatures and effective moments extracted from Curie-Weiss plots of inverse susceptibility vs temperature from 150 K to 400 K for the single phase $Sr_{2-x}Ba_xNiOsO_6$ samples.

Composition (x)	Structure (300 K)	Weiss temperature (K)	Effective moment (μ_B)
0.2	*I4/m*	24	3.64
0.4	*I4/m*	41	3.61
0.6	*I4/m*	50	3.64
0.8	$Fm\bar{3}m$	68	3.61
1.0	$Fm\bar{3}m$	75	3.50
1.2	$Fm\bar{3}m$	79	3.61
2.0	$P\bar{3}m1$	−18	3.85

Ba_2NiOsO_6 orders ferrimagnetically (T_C = 108 K), with a magnetic structure where both the Os^{6+} spins and the Ni^{2+} spins are ferrimagnetic in nature. In this magnetic structure the ~180° Ni–O–Os superexchange

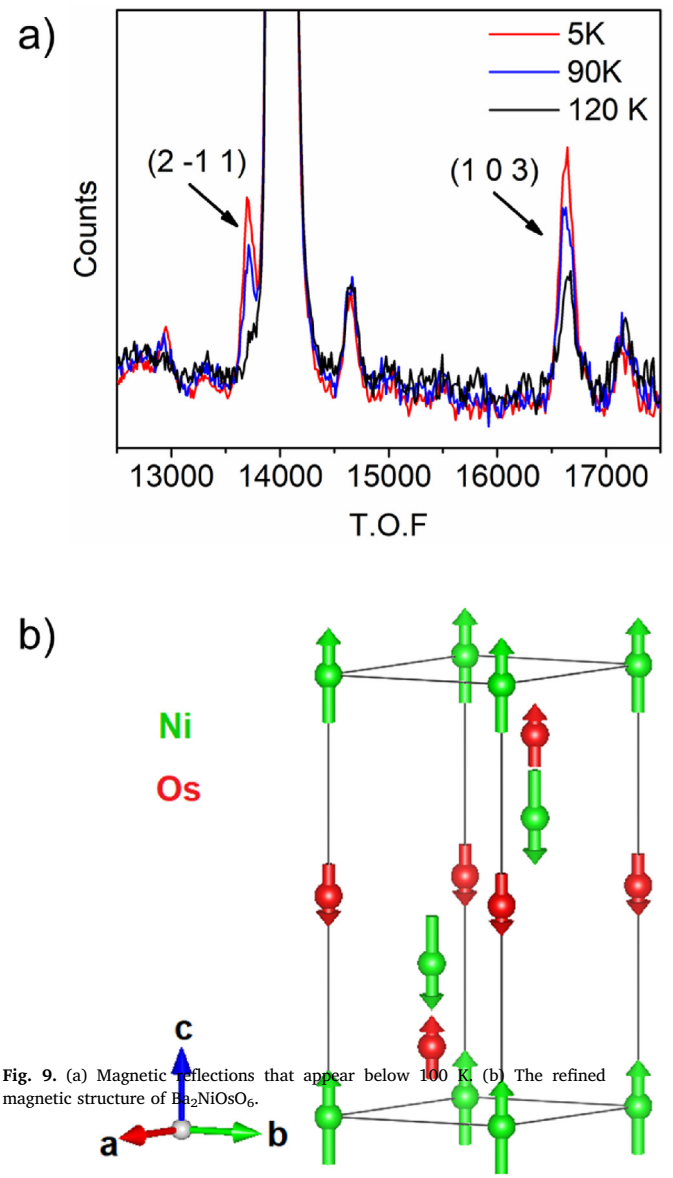

Fig. 9. (a) Magnetic reflections that appear below 100 K. (b) The refined magnetic structure of Ba_2NiOsO_6.

coupling is ferromagnetic and the ~90° Ni–O–Os coupling is antiferromagnetic. The signs of both interactions agree with the predictions of the Goodenough-Kanamori rules. From this we conclude that superexchange interactions between 3d and 5d ions follow the predictions of the Goodenough-Kanamori rules provided the t_{2g} orbitals of the 3d ion are completely filled and competing superexchange interactions are suppressed.

CRediT authorship contribution statement

Phuong M. Tran: Data curation, Formal analysis, Investigation, Writing - original draft. John S.O. Evans is responsible for investigation, data analysis, and editing and revising the manuscript. Patrick M. Woodward is responsible for conceiving the project, project administration, editing and revising the manuscript.

Declaration of competing interest

The authors declare that they have no known competing financial interests or personal relationships that could have appeared to influence the work reported in this paper.

Data availability

Data will be made available on request.

Acknowledgement

Support for this research was provided by the Center for Emergent Materials, an NSF Materials Research Science and Engineering Center (DMR-2011876). Work at Oak Ridge National Laboratory was supported by the US Department of Energy, Office of Science, Basic Energy Sciences, Materials Sciences and Engineering Division, under contract number DE-AC05-00OR22725.

Appendix A. Supplementary data

Supplementary data to this article can be found online at https://doi.org/10.1016/j.jssc.2022.123667.

References

[1] Y. Krockenberger, K. Mogare, M. Reehuis, M. Tovar, M. Jansen, G. Vaitheeswaran, V. Kanchana, F. Bultmark, A. Delin, F. Wilhelm, A. Rogalev, A. Winkler, L. Alff, Phys. Rev. B 75 (2007), 020404. R.
[2] R. Morrow, J.R. Soliz, A.J. Hauser, J.C. Gallagher, M.A. Susner, M.D. Sumption, A.A. Aczel, J. Yan, F. Yang, P.M. Woodward, The effect of chemical pressure on the structure and properties of A_2CrOsO_6 (A = Sr, Ca) ferrimagnetic double perovskites, J. Solid State Chem. 238 (2016) 46–52.
[3] H.L. Feng, M.P. Ghimire, Z. Hu, S.-C. Liao, S. Agrestini, J. Chen, Y. Yuan, Y. Matsushita, Y. Tsujimoto, Y. Katsuya, M. Tanaka, H.-Ji Lin, C.-T. Chen, S.-C. Weng, M. Valvidares, K. Chen, F. Baudelet, A. Tanaka, M. Greenblatt, L.H. Tjeng, K. Yamaura, Room temperature ferrimagnetism of antisite disordered Ca_2MnOsO_6, Phys. Rev. Mater. 3 (2019), 124404.
[4] J.B. Goodenough, Theory of the role of covalence in the perovskite-type manganites [La,M(II)]MnO_3, Phys. Rev. 100 (1955) 564.
[5] A.K. Paul, M. Jansen, B. Yan, C. Felser, M. Reehuis, P.M. Abdala, Synthesis, crystal structure and physical properties of Sr_2FeOsO_6, Inorg. Chem. 52 (2013) 6713–6719.
[6] A.K. Paul, M. Reehuis, V. Ksenofontov, B. Yan, A. Hoser, D.M. Többens, P.M. Abdala, P. Adler, M. Jansen, C. Felser, Lattice instability and competing spin structures in the double perovskite insulator Sr_2FeOsO_6, Phys. Rev. Lett. 111 (2013), 167205.
[7] R. Morrow, R. Mishra, O.D. Restrepo, M.R. Ball, W. Windl, S. Wurmehl, U. Stockert, B. Büchner, P.M. Woodward, Independent ordering of two interpenetrating magnetic sublattices in the double perovskite Sr_2CoOsO_6, J. Am. Chem. Soc. 135 (2013) 18824–18830.
[8] A.K. Paul, M. Reehuis, C. Felser, P.M. Abdala, M. Jansen, Synthesis, crystal structure, and properties of the ordered double perovskite Sr_2CoOsO_6, Z. Anorg. Allg. Chem. 639 (2013), 2431-2425.
[9] B.H. Yan, A.K. Paul, S. Kanungo, M. Reehuis, A. Hoser, D.M. Többens, W. Schelle, R.C. Williams, T. Lancaster, F. Xiao, J.S. Moller, S.J. Blundell, W. Hayes, C. Felser, M. Jansen, Lattice-site-specific spin dynamics in double perovskite Sr_2CoOsO_6, Phys. Rev. Lett. 112 (2014), 147202.
[10] R. Macquart, S.-J. Kim, W.R. Gemmill, J.K. Stalick, Y. Lee, T. Vogt, H.-C. zur Loye, Synthesis, structure, and magnetic properties of Sr_2NiOsO_6 and Ca_2NiOsO_6: two new osmium-containing double perovskites, Inorg. Chem. 44 (2005) 9676–9683.
[11] H.L. Feng, S. Calder, P. Ghimire, Y. Yuan, Y. Shirako, M.P. Ghimire, Y. Yuan, Y. Shirako, Y. Tsujimoto, Y. Matsushita, Z. Hu, C. Kuo, L.H. Tjeng, T. Pi, Y. Soo, J. He, M. Tanaka, Y. Katsuya, M. Richter, K. Yamaura, Ba_2NiOsO_6: a Dirac-Mott insulator with ferromagnetism near 100 K, Phys. Rev. B 94 (2016), 235158.
[12] R.C. Morrow, J.W. Freeland, P.M. Woodward, Probing the links between structure and magnetism in $Sr_{2-x}Ca_xFeOsO_6$ double perovskites, Inorg. Chem. 53 (2014) 7398–7992.
[13] R. Morrow, J. Yan, M.A. McGuire, J.W. Freeland, D. Haskel, P.M. Woodward, Effects of chemical pressure on the magnetic ground states of the osmate double perovskites $SrCaCoOsO_6$ and Ca_2CoOsO_6, Phys. Rev. B 92 (2015), 094435.
[14] R. Morrow, K. Samanta, T. Saha-Dasgupta, J. Xiong, J.W. Freeland, D. Haskel, P.M. Woodward, Magnetism in Ca_2CoOsO_6 and Ca_2NiOsO_6: unravelling the mystery of superexchange interactions between 3d and 5d ions, Chem. Mater. 28 (2016) 3666–3675.
[15] V.M. Goldschmidt, Die gesetze der Krystallochemie, Naturwissenschaften 14 (1926) 477–485.
[16] A. Cohelo, TOPAS-Academic, Powder Diffr. (2007) 312–317.
[17] B.H. Toby, EXPGUI, a graphical user interface for GSAS, J. Appl. Crystallogr. 34 (1991) 210–213.
[18] P.W. Barnes, M.W. Lufaso, P.M. Woodward, Structure determination in A2M3+M5+O6 and A2M2+M6+O6 ordered perovskites: octahedral tilting and pseudosymmetry, Acta Crystallogr. B 62 (2006) 384–396.
[19] H. Liu, S. Gonzalez, Mater. Res. Soc. Symp. Proc. 48 (2007) 329–330.

[20] Y. Tanga, R.P. Sena, M. Avdeev, P.D. Battle, J.M. Cadogan, J. Hadermann, E.C. Hunter, Magnetic properties of the 6H perovskite $Ba_3Fe_2TeO_9$, J. Solid State Chem. 253 (2017) 347–354.
[21] H.L. Feng, P. Adler, M. Reehuis, W. Schnelle, P. Pattison, A. Hoser, C. Felser, M. Jansen, High-temperature ferrimagnetism with large coercivity and exchange bias in the partially ordered 3d/5d hexagonal perovskite $Ba_2Fe_{1.12}Os_{0.88}O_6$, Chem. Mater. 29 (2017) 886–895.
[22] U. Treiber, S. Kemmler-Sack, Untersuchungen an hexagonalen 6L-Perowskiten $Ba_2B^{II}OsO_6$ mit B^{II} = Co, Ni, Z. Anorg. Allg. Chem. 470 (1980) 95.
[23] B.J. Campbell, H.T. Stokes, D.E. Tanner, D.M. Hatch, ISODISPLACE: a web based tool for exploring structural distortions, J. Appl. Crystallogr. 39 (2006) 607–614.
[24] M.J. Martínez-Lope, J.A. Alonso, M.T. Casais, Synthesis, crystal and magnetic structure of the double perovskites A_2NiMoO_6 (A = Sr, Ba): a neutron diffraction study, Eur. J. Inorg. Chem. 6 (2003) 2839–2844.